Spatiotemporal Splitting of Global Eigenmodes due to Cross-Field Coupling via Vortex Dynamics in Drift Wave Turbulence

C. Brandt,[1,*] S. C. Thakur,[1,2] A. D. Light,[2,3] J. Negrete, Jr.,[4] and G. R. Tynan[1,2]
[1]*Center for Energy Research, University of California—San Diego, La Jolla, California 92093-0417, USA*
[2]*Center for Momentum Transport and Flow Organization, La Jolla, California 92093-0417, USA*
[3]*Center for Integrated Plasma Studies, Department of Physics, University of Colorado at Boulder, Boulder, Colorado 80309, USA*
[4]*Max-Planck-Institut für Dynamik und Selbstorganisation (MPIDS), Am Faßberg 17, 37077 Göttingen, Germany*

(Received 21 March 2014; published 29 December 2014)

Spatiotemporal splitting events of drift wave (DW) eigenmodes due to nonlinear coupling are investigated in a cylindrical helicon plasma device. DW eigenmodes in the radial-azimuthal cross section have been experimentally observed to split at radial locations and recombine into the global eigenmode with a time shorter than the typical DW period ($t \ll f_{\mathrm{DW}}^{-1}$). The number of splits correlates with the increase of turbulence. The observed dynamics can be theoretically reproduced by a Kuramoto-type model of a network of radially coupled azimuthal eigenmodes. Coupling by $E \times B$—vortex convection cell dynamics and ion gyro radii motion leads to cross-field synchronization and occasional mode splitting events.

DOI: 10.1103/PhysRevLett.113.265001 PACS numbers: 52.25.Xz, 05.45.Xt, 52.35.Kt, 52.35.Mw

Nonlinear coupling leads to complex dynamics like synchronization, chaos, and broadband turbulence in fluids and plasmas. In magnetized plasmas the pressure-gradient-driven drift wave (DW) instability is a paradigm for nonlinear mode-mode coupling. Nonlinearly generated DW vortices lead to cross-field transport and plasma turbulence [1,2]. Because of energy transfer via inverse cascades by quasi-2D dynamics [3], large scale structures can be formed out of turbulence [4,5]. Global eigenmode formation is common not only in plasma physics, but also in quasi-2D fluid dynamical systems with an axis of rotational symmetry [6]. A detailed understanding of the development of coherent structures out of an underlying instability is of fundamental interest in self-organization [7] and pattern formation [8].

Experiments in cylindrical geometry have long been used to study the DW and the transition to turbulence [9–13]. Depending on operation parameters and boundary conditions, coherent eigenmodes, nonlinearly coupled modes, and broadband turbulence can all be observed [14–17]. This Letter reports experimental observations of spatiotemporal mode splitting of "global," i.e., spatially extended coherent, DW eigenmodes and a theoretical model that reproduces this phenomenon. With increasing turbulent dynamics, the global eigenmodes more frequently shear apart for a time interval $t \ll f_{\mathrm{DW}}^{-1}$. Standard models of DWs (e.g., Hasegawa-Wakatani) are unable to predict or explain these mode splitting events. The quasistability of the global mode structure can be understood by an ensemble of nonlinearly coupled eigenmodes. A standard Kuramoto-type model of coupled oscillators [18,19] is modified by adding both self- and mutual-mode coupling. The basic plasma physics is incorporated through the nonlinear coupling terms, which are calculated from experimentally measured local DW dispersion relations and modeled $E \times B$—vortex dynamics. Cross-field synchronization leads to the formation of quasistable global eigenmodes that undergo mode splitting events via phase slippages.

The experiments were performed in the cylindrical CSDX device [13] (length 2.8 m, radius 0.1 m) which produces a sharply peaked [20] magnetized argon plasma using an $m = 0$ helicon antenna (radius 7.5 cm). Typical operating parameters are 1.6 kW rf input power and gas pressure of 0.42 Pa. Radially movable multitip Langmuir probes [21] are used to measure radial profiles of standard plasma parameters and vorticity [22]. The intensity of visible light in the azimuthal cross section is measured by a Phantom V710 high speed camera using filters for detecting emission from neutrals and ions [23]. The focal plane is imaged by a telescope setup onto the camera chip [depth of field (DOF) ~10 cm, parallax $< 0.5°$] [23,24]. $\tilde{E} \times B$—vorticity fluctuations ($\tilde{\Omega} = \nabla \times \tilde{v}_{E\times B}$) are measured with a 3×3 probe array [21] and are associated with light intensity fluctuations (zero-lag correlation values of ≈0.5–0.8). Light fluctuations represent the dynamics of density fluctuations [25] and the dynamics of $\tilde{E} \times B$ vorticity [26].

In the studied magnetic field range of $B = 40$–240 mT, the pressure driven DW instability dominates the dynamics in the density gradient region ($r = 1$–6 cm) [24] with $\omega_{\mathrm{DW}} < k_{\parallel} v_{T_e}$. Azimuthal FFT decomposition of the camera images is used to obtain azimuthal eigenmodes [27–37]. Radial profiles of the light fluctuation amplitude and the azimuthal angle (phase) are mode-selectively extracted to study the temporal evolution of the 2D structure of eigenmodes. In weakly developed turbulence (at $B = 90$ mT), global eigenmodes propagate and split

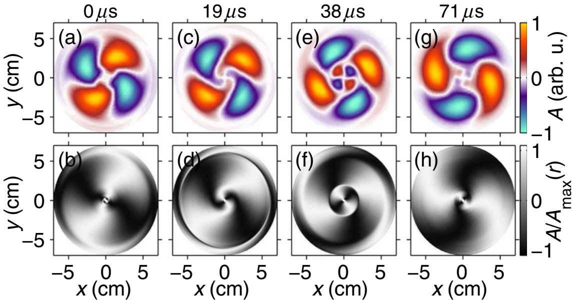

FIG. 1 (color online). Temporal evolution of a mode splitting event of an $m = 2$ mode ($f_{\mathrm{DW}} \sim 4.9$ kHz, $B = 90$ mT). The bottom row shows the mode structure normalized to the azimuthal mode amplitude for each radius to visualize mode splits in low amplitude regions.

occasionally in time intervals $< 0.2 f_{\mathrm{DW}}^{-1}$. In CSDX, for these parameters, the eigenmodes $m = 1, 2, 3$ are dominant [13,38,39]. For example, we show the dynamics of the $m = 2$ mode (a similar dynamics is observed for $m = 1$ and $m = 3$). Figure 1 shows a clockwise-propagating $m = 2$ mode as it undergoes a radial mode splitting event. At $t = 0$ the mode structure is globally coherent [Figs. 1(a) and 1(b)]. Within a quarter period, the mode structure undergoes a complete split and recombination: at a radius of $r \sim 2$ cm, the inner mode structure propagates slightly backwards ($t = 19$ μs) and splits at $t = 38$ μs while the outer mode continues its propagation. Eventually the inner and outer eigenmode structures recombine [Figs. 1(g) and 1(h)]. Mode splitting is observed at various radii; however, the events are predominantly observed close to the core and in the edge region. In Figs. 1(d) and 1(f) mode splits happen at $r \sim 1$ cm and at $r \sim 6$ cm. Figure 2 illustrates the temporal evolution of azimuthal phases at two slightly different radial positions. According to the propagation of the mode structure, the azimuthal phases increase in time for both positions [Fig. 2(a)] with an angular velocity according to the Doppler-shifted electron diamagnetic drift at each radius. The velocity $\partial_t \theta$ is not constant in time, however, and the phase difference between two radially separated eigenmodes [Fig. 2(b)] reveals discrete steps of 2π known as *phase slippages*. With the definition $\Delta\theta = \theta(r_2) - \theta(r_1)$ (with $r_2 > r_1$), phase slippages are predominantly positive close to the core region and negative in the edge region. Figures 2(c) and 2(d) show a detailed time interval with three typical phase slippages. Sometimes a slippage starts to evolve but then the phase difference is pulled back [Fig. 2(d)]. In the following we call such events “phase pulling.” The mode amplitudes (∼vorticity) decrease at both radial positions during phase slippages and phase pulling [Fig. 2(e)]. Figure 3 compares the dynamics of phase slippages and phase pulling. For phase pulling the outer mode starts to accelerate and the inner mode follows with a time lag of $\tau \sim 10$ μs. This behavior results in a temporary nonzero phase difference [Figs. 3(a) and 3(b)] and velocity increase for the outer and inner modes [Fig. 3(c)]. For phase slippages, the modes accelerate in opposite directions [Fig. 3(f)]. One mode accelerates until the phase difference again becomes small (passing through 2π) and then decelerates (the other first decelerates and then accelerates). After the phase slippage both modes again propagate with the same velocity.

The effective frequency of uncoupled DWs corresponds to the $E \times B$-Doppler-shifted electron diamagnetic drift [3] $\omega(r, m) = \omega^*(r, m) + m\omega_{E\times B}(r)$, with $\omega^* = -k_{\mathrm{B}} T_{\mathrm{e}} k_\perp (eB(1 + k_\perp^2 \rho_{\mathrm{s}}^2))^{-1} (\partial_r \ln n_{\mathrm{e}} + \partial_r \ln T_{\mathrm{e}})$, k_{B} being the Boltzmann constant, $T_{\mathrm{e}}(r)$ the electron temperature, e the elementary charge, B the magnetic induction, $\rho_{\mathrm{s}} = \{m_{\mathrm{i}} T_{\mathrm{e}}/(eB^2)\}^{1/2}$ the drift scale, m_{i} the ion mass, $k_\perp(r, m) = m/r$ the perpendicular wave number, $n_{\mathrm{e}}(r)$ the density, and $\omega_{E\times B} = -(Br)^{-1} \partial_r \phi(r)$ and $\phi(r)$ the plasma potential. The radial profiles of $\omega(r, m)$

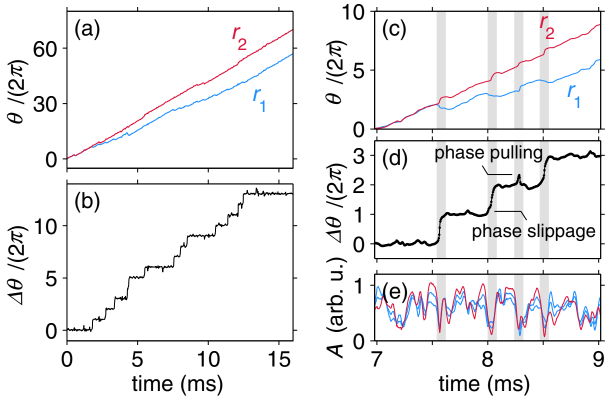

FIG. 2 (color online). Temporal evolution of (a) the azimuthal phases of an $m = 2$ mode at two different radii and (b) the difference $\theta_2 - \theta_1$. Diagrams (c) and (d) show an enlarged part of the time traces of diagrams (a) and (b), and (e) shows the mode amplitude. In diagrams (a) and (c) initial phases are set to $\theta_1 = \theta_2 = 0$ ($r_1 = 2.0$ cm, $r_2 = 2.6$ cm).

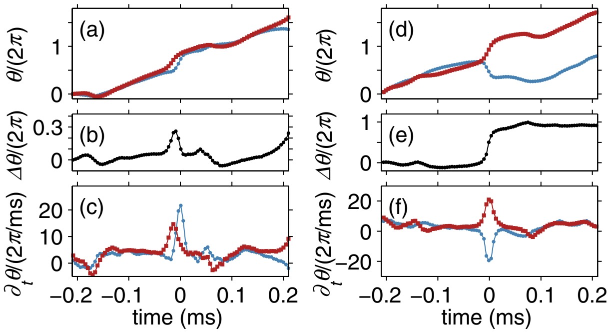

FIG. 3 (color online). Temporal evolution of the phase (top panels), phase difference (center panels), and phase velocity (bottom panels) of an $m = 2$ mode at two different radii for phase pulling (left panels) and a phase slippage (right panels). $r_2 > r_1$, r_1: blue circles, r_2: red squares.

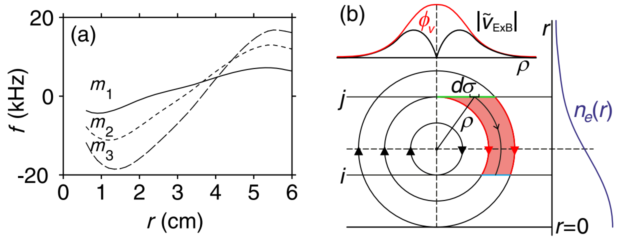

FIG. 4 (color online). (a) Doppler-shifted dispersion relation $f = \omega(r,m)/(2\pi)$ from measured average profiles of ϕ, n_e, and T_e. (b) $E \times B$—vortex coupling model. ρ: radial coordinate of the vortex, $\phi_v(\rho)$: vortex potential profile, $d\sigma$: part of the secant (green lines) of the radial oscillator at r_j.

[Fig. 4(a)] are obtained from experimentally measured radial profiles of n_e, ϕ, and T_e [24].

In the following the phase dynamics of global eigenmodes is modeled by a network of Kuramoto-type phase-coupled azimuthal eigenmodes (oscillators) [18]. For each mode number m, a radial set of N (here $N = 100$) radially coupled azimuthal eigenmodes is considered. The temporal evolution of the azimuthal phase θ_{mi} at a radial position r_i ($1 \leq i \leq N$) is given by

$$\frac{\partial \theta_{mi}}{\partial t} = \omega_{mi} + \sum_{l=1}^{M} \sum_{j \neq i}^{N} K_{mi,lj} \sin(\theta_{lj} - \theta_{mi}), \qquad (1)$$

with ω_{mi} being the eigenfrequency of the ith oscillator of mode m and $K_{mi,lj}$ the coupling strength between the jth oscillator of mode l and the ith oscillator of mode m. The sum of index j is the contribution of radial coupling from mode l (summed over M eigenmodes) at position r_j to mode m at r_i. For $l = m$ the coupling matrix $K_{mi,lj}$ describes the radial self-coupling of an eigenmode, and for $l \neq m$ it represents mutual mode coupling. The eigenfrequencies ω_{mi} are calculated from the experimentally measured DW dispersion $\omega(r,m)$ [Fig. 4(a)]. It is assumed that the qualitative structure of the radial coupling matrices is the same for self-coupling and for mode-mode coupling. The matrices differ only by a constant factor A_{ml}, i.e., $K_{mi,lj} = A_{ml} K_{ij}$ (caused by the larger overlap of a mode with itself; we assume $A_{m=l} > A_{m\neq l}$).

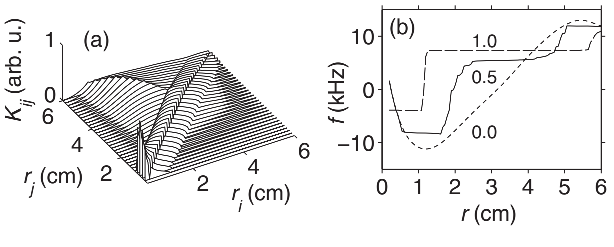

FIG. 5. (a) Coupling coefficient matrix and (b) averaged radial frequency profiles of the $m = 2$ mode in the Kuramoto model for three different coupling amplitudes a_0 with $a_0 K_{mi,lj}$.

The underlying physics is included in the coupling coefficient matrix K_{ij}. Significant coupling of azimuthal eigenmodes results from cross-field drifts and ion gyration. We include $E \times B$—vortex coupling (V_{ij}) and ion gyro radius coupling (G_{ij}) with $K_{ij} = (V_{ij} + G_{ij})(r_j/r_i)$, where r_j/r_i considers the circumference ratio of azimuthal eigenmodes. (Coupling due to the ion polarization drift is neglected in this model since $|v_{E\times B}|/|v_{\mathrm{pol,i}}| \sim \omega_{\mathrm{ci}}/\omega_{\mathrm{DW}} \gg 1$.) The potential perturbation corresponding to a DW creates cross-field plasma transport by $E \times B$—vortex dynamics. Consequently, azimuthal DW eigenmodes at different radii are mutually interacting by cross-field plasma flows. According to the observed correlation between decrease of vorticity ($\sim E \times B$ coupling) and phase slippages [Fig. 2(e)], it is assumed that the coupling strength scales with vorticity. Figure 4(b) shows a simple illustration of how V_{ij} is calculated. As a measure for the coupling strength from an oscillator at r_j to an oscillator at r_i, the particle flux within the vortex from r_j to r_i is calculated within the red trajectories of Fig. 4(b). The coupling matrix is calculated by $V_{ij} = \int \Gamma_{n,j} e^{-t_{ij}/\tau} d\sigma$, where $\Gamma_{n,j} = \tilde{n}(r_j) \cdot \tilde{v}_{E\times B}(\rho)$, with $\tilde{n}(r_j)$ being the density fluctuations at radius r_j and $\tilde{v}_{E\times B}(\rho)$ the vortex velocity at the distance ρ from the vortex center. The time the plasma element takes to travel from r_j to r_i is $t_{ij} \sim l_{ij}/\tilde{v}_{E\times B}$, where l_{ij} is the length along the trajectory. The lifetime of a perturbation is assumed to be $\tau \sim \rho_s/v_{\mathrm{th,i}}$ (about 50 μs in the model), with $v_{\mathrm{th,i}}$ being the thermal ion velocity. The ion gyro radius r_{ci} is of the order of $\sim$0.5 cm for $T_i \sim 0.4$ eV [40]. Ion gyro radius coupling from r_j to r_i is assumed to be proportional to the ion flux, i.e., $G_{ij} = n(r_j) v_{\mathrm{th,i}} \sin(\alpha)$, with $\alpha = \arccos(|r_i - r_j|/r_{\mathrm{ci}})$ being the angle between the ion trajectory centered at r_j and the oscillator plane at r_i. The corresponding coupling matrix is depicted in Fig. 5(a). $E \times B$—vortex coupling results in the flat pattern spread across the whole radial range. The structure around $r_i \sim r_j$ is from ion gyro radius coupling exhibiting a short effective coupling range of $\sim r_{\mathrm{ci}}$.

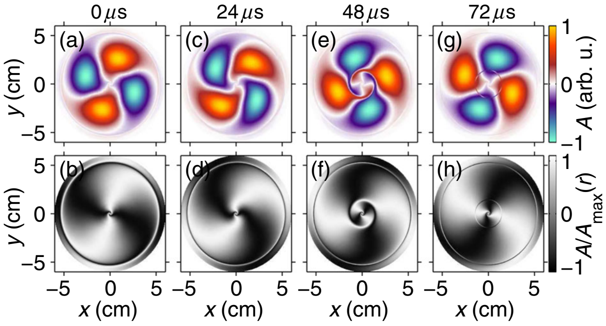

FIG. 6 (color online). Cross-sectional dynamics of the $m = 2$ mode modeled by a Kuramoto model including two coupled modes ($m = 1, 2$). The bottom row shows the mode structure normalized to the azimuthal mode amplitude for each radius to visualize mode splits in low amplitude regions.

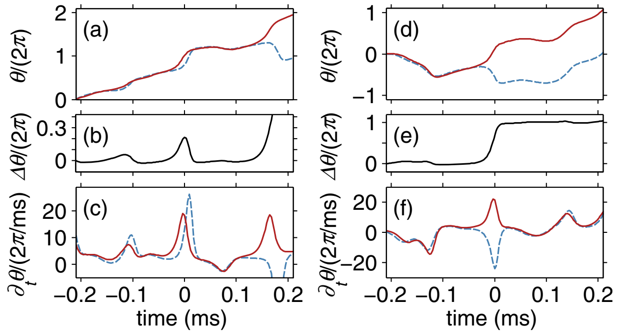

FIG. 7 (color online). Phase pulling (left panels) and phase slippage (right panels) obtained from Kuramoto-type phase coupling. Temporal evolution of (a),(d) the phase, (b),(e) the phase difference, and (c),(f) the phase velocity. Blue dashed lines: r_2, red solid lines: r_2, with $r_2 > r_1$.

Comparing Fig. 4(a) with Fig. 5(b) shows the importance of the coupling terms. Figure 5(b) depicts the averaged phase velocities of the $m = 2$ mode for different coupling strengths. Without coupling, the model reflects only the eigenfrequencies $\omega(r, m)$. With nonzero coupling coefficients, radially extended regions of equal phase velocity are formed. Measurements of radial profiles of density and potential fluctuations show similarly extended regions of constant frequency [24]. The larger the coupling strength, the broader the phase-synchronized regions become. According to the Doppler-shifted dispersion relation [Fig. 4(a)] of uncoupled DW modes, no stable global eigenmodes would form. However, the mutual synchronization of azimuthal eigenmodes at different radii results in the formation of global azimuthal eigenmodes.

This is the first model which can reproduce the observed eigenmode splitting events shown in Fig. 1. Figure 6 depicts the phase dynamics of the $m = 2$ mode obtained from the Kuramoto model, including self-coupling and mutual mode coupling between the modes $m = 1, 2, 3$. The radial amplitude dependence is taken to be the average experimental amplitude profile. The model shows the formation of global radial-azimuthal eigenmodes [Fig. 6(a) shows the $m = 2$ mode] due to synchronization through cross-field radial coupling. Similar to the experimental observations in Fig. 1, mode splits of the global mode frequently occur at outer radii [Figs. 6(a) and 6(b)] and inner radii [Figs. 6(e) and 6(f)]. After a mode split the mode structure recombines to the global eigenmode [Figs. 6(g) and 6(h)].

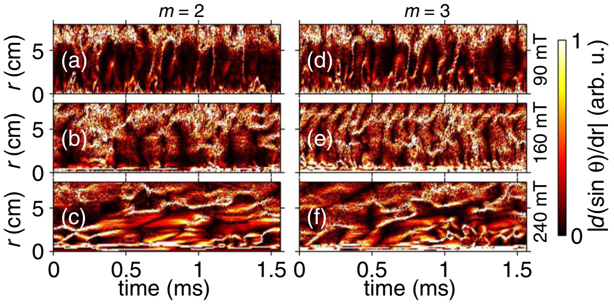

FIG. 8 (color online). Radial and temporal evolution of mode splitting events exemplarily for $m = 2$ and $m = 3$ from (top panels) weak to (bottom panels) broadband turbulence. Black structures correspond to regions of radial stable modes; white structures represent mode splits.

Figure 7 shows modeled phase traces from nearby radial locations, demonstrating a phase pulling and a phase slippage event. The modeled phase traces are highly similar to those obtained from measurement [Fig. 3]. The details of both phase pulling events and phase slippages are reproduced [compare Figs. 7(b) and 7(e) with Figs. 3(b) and 3(e)] and the phase velocities agree qualitatively and quantitatively [compare Figs. 7(c) and 7(f) with Figs. 3(c) and 3(f)].

Experimental results show that the mode split dynamics correlate with increasing turbulence [Fig. 8]. In weakly developed turbulence [Figs. 8(a) and 8(d)] mode splits mostly occur in the core and edge regions. With increasing turbulent dynamics (increasing B) the number of mode splits increase temporally and spatially [Figs. 8(b), 8(c), 8(e), and 8(f)].

Signatures of mode splits were first anticipated in Ref. [27]; however, because of the strong parallax in that experiment, it could not be unambiguously verified and studied. Moreover since the radial and axial motion could not be decoupled clearly, the effect of radial coupling was not found. Comparison of a Kuramoto-type phase coupling model with experimental observations suggests that radial cross-field coupling is essential for the formation of global DW eigenmodes. The model predicts the detailed phase dynamics of mode splitting events. Experiments indicate that mode splits are correlated with turbulence. Cross-field coupling via $E \times B$—vortex dynamics may also occur in poloidal-toroidal DW eigenmodes in toroidal confinement devices. Vortex dynamics may, in general, result in long-range cross-field coupling and can often play a significant role in pattern formation, synchronization, and self-organization independent of geometry.

This work was supported by U.S. DOE Grants No. DE-FG02-07ER54912, No. DE-FG02-OER54871, and No. DE-SC0008378.

---

*c.brandt@fz-juelich.de

[1] W. Horton, Rev. Mod. Phys. **71**, 735 (1999).
[2] G. R. Tynan, A. Fujisawa, and G. McKee, Plasma Phys. Controlled Fusion **51**, 113001 (2009).
[3] A. Hasegawa and K. Mima, Phys. Rev. Lett. **39**, 205 (1977).
[4] A. Hasegawa and Y. Kodama, Phys. Rev. Lett. **41**, 1470 (1978).
[5] P. Manz, G. Birkenmeier, M. Ramisch, and U. Stroth, Phys. Plasmas **19**, 082318 (2012).

[6] S. R. Maassen, H. J. H. Clercx, and G. J. F. van Heijst, Europhys. Lett. **46**, 339 (1999).

[7] G. Nicolis and I. Prigogine, *Self-Organization in Nonequilibrium Systems* (John Wiley & Sons, New York, 1977).

[8] M. C. Cross and P. C. Hohenberg, Rev. Mod. Phys. **65**, 851 (1993).

[9] R. F. Ellis, E. Marden-Marshall, and R. Majeski, Plasma Phys. **22**, 113 (1980).

[10] T. Klinger, A. Latten, A. Piel, G. Bonhomme, T. Pierre, and T. Dudok de Wit, Phys. Rev. Lett. **79**, 3913 (1997).

[11] T. Klinger, A. Latten, A. Piel, G. Bonhomme, and T. Pierre, Plasma Phys. Controlled Fusion **39**, B145 (1997).

[12] E. Gravier, X. Caron, G. Bonhomme, and T. Pierre, Phys. Plasmas **6**, 1670 (1999).

[13] M. J. Burin, G. R. Tynan, G. Y. Antar, N. A. Crocker, and C. Holland, Phys. Plasmas **12**, 052320 (2005).

[14] C. Schröder, O. Grulke, T. Klinger, and V. Naulin, Phys. Plasmas **11**, 4249 (2004).

[15] F. Brochard, T. Windisch, O. Grulke, and T. Klinger, Phys. Plasmas **13**, 122305 (2006).

[16] O. Grulke, S. Ullrich, T. Windisch, and T. Klinger, Plasma Phys. Controlled Fusion **49**, B247 (2007).

[17] S. C. Thakur, M. Xu, P. Manz, N. Fedorczak, C. Holland, and G. R. Tynan, Phys. Plasmas **20**, 012304 (2013).

[18] Y. Kuramoto, *Chemical Oscillations, Waves and Turbulence* (Dover Publications, New York, 2003).

[19] J. A. Acebrón, L. L. Bonilla, C. J. Pérez Vicente, F. Ritort, and R. Spigler, Rev. Mod. Phys. **77**, 137 (2005).

[20] C. M. Franck, O. Grulke, and T. Klinger, Phys. Plasmas **10**, 323 (2003).

[21] M. Xu, G. R. Tynan, C. Holland, Z. Yan, S. H. Müller, and J. H. Yu, Phys. Plasmas **16**, 042312 (2009).

[22] W. Horton, J. C. Perez, T. Carter, and R. Bengtson, Phys. Plasmas **12**, 022303 (2005).

[23] A. D. Light, S. C. Thakur, C. Brandt, Y. Sechrest, G. R. Tynan, and T. Munsat, Phys. Plasmas **20**, 082120 (2013).

[24] S. C. Thakur, C. Brandt, L. Cui, J. J. Gosselin, A. D. Light, and G. R. Tynan, Plasma Sources Sci. Technol. **23**, 044006 (2014).

[25] S. Oldenbürger, C. Brandt, F. Brochard, N. Lemoine, and G. Bonhomme, Rev. Sci. Instrum. **81**, 063505 (2010).

[26] M. Xu, G. R. Tynan, P. H. Diamond, C. Holland, J. H. Yu, and Z. Yan, Phys. Rev. Lett. **107**, 055003 (2011).

[27] C. Brandt, O. Grulke, T. Klinger, J. Negrete, Jr., G. Bousselin, F. Brochard, G. Bonhomme, and S. Oldenbürger, Phys. Rev. E: Stat., Nonlinear, Soft Matter Phys. **84**, 056405 (2011).

[28] A. Latten, T. Klinger, A. Piel, and T. Pierre, Rev. Sci. Instrum. **66**, 3254 (1995).

[29] C. Schröder, T. Klinger, D. Block, A. Piel, G. Bonhomme, and V. Naulin, Phys. Rev. Lett. **86**, 5711 (2001).

[30] C. Brandt, O. Grulke, and T. Klinger, Plasma Phys. Controlled Fusion **52**, 055009 (2010).

[31] C. Brandt, O. Grulke, and T. Klinger, Phys. Plasmas **17**, 032304 (2010).

[32] F. Brochard, G. Bonhomme, E. Gravier, S. Oldenbürger, and M. Philipp, Phys. Plasmas **13**, 052509 (2006).

[33] T. Yamada, S.-I. Itoh, T. Maruta, N. Kasuya, Y. Nagashima, S. Shinohara, K. Terasaka, M. Yagi, S. Inagaki, Y. Kawai, S. Fujisawa, and K. Itoh, Nature (London) **4**, 721 (2008).

[34] S. J. Zweben and R. W. Gould, Nucl. Fusion **25**, 171 (1985).

[35] G. Birkenmeier, M. Ramisch, G. Fuchert, A. Köhn, B. Nold, and U. Stroth, Plasma Phys. Controlled Fusion **55**, 015003 (2013).

[36] M. Ramisch, E. Häberle, N. Mahdizadeh, and U. Stroth, Plasma Sources Sci. Technol. **17**, 024007 (2008).

[37] See Supplemental Material at http://link.aps.org/supplemental/10.1103/PhysRevLett.113.265001, which includes Refs. [14,28–36], for details about azimuthal FFT mode decomposition and azimuthal phase extraction.

[38] G. R. Tynan, C. Holland, J. H. Yu, A. James, D. Nishijima, M. Shimada, and N. Taheri, Plasma Phys. Controlled Fusion **48**, S51 (2006).

[39] P. Manz, M. Xu, S. C. Thakur, and G. R. Tynan, Plasma Phys. Controlled Fusion **53**, 095001 (2011).

[40] S. C. Thakur, D. McCarren, T. Lee, N. Fedorczak, P. Manz, E. E. Scime, G. R. Tynan, and M. Xu, Phys. Plasmas **19**, 082102 (2012).